PHYSICAL REVIEW B **82**, 054112 (2010)

Pyroelectric scanning probe microscopy: A method for local measurement of the pyroelectric effect in ferroelectric thin films

J. Groten,[1] M. Zirkl,[1] G. Jakopic,[1] A. Leitner,[2] and B. Stadlober[1,*]
[1]*Joanneum Research, Institute of Nanostructured Materials and Photonics, 8160 Weiz, Austria*
[2]*Institute of Physics, Karl-Franzens University Graz, 8010 Graz, Austria*
(Received 11 March 2010; revised manuscript received 22 May 2010; published 18 August 2010)

This work demonstrates a surface scanning method for the quantitative determination of the local pyroelectric coefficient in ferroelectric thin films. It allows generating a map of the pyroelectric response with very high spatial resolution. In domains of previously aligned dipole moments (achieved by tip-assisted poling) small heat fluctuations are achieved by laser diode excitation from the sample's bottom side thus inducing changes in the surface potential due to the pyroelectric effect. Simultaneously, the surface potential variations are detected by scanning surface potential microscopy thus forming the base for the pyroelectric coefficient map. The potential of the method is demonstrated on the basis of ferroelectric semicrystalline copolymer thin films yielding local maxima of the pyroelectric coefficients up to 40 $\mu C/m^2$ K. Another promising feature is the ability to visualize "screened" polarization thus enabling in-depth profiling of polarization distributions and domain formation and to study the composition dependence of ferroelectric nanodomains.

DOI: 10.1103/PhysRevB.82.054112 PACS number(s): 68.37.Ps, 77.55.Kt, 81.16.Nd

I. INTRODUCTION

The interest in the fundamental nature of spontaneous order in ferroelectric materials has motivated a large number of scanning probe microscopy (SPM) studies, most of them dedicated to detect the local spontaneous polarization and its piezoelectric response.[1] Although pyroelectricity is a more general effect than ferroelectricity[2] and, moreover, is a main topic in noncooled infrared (IR) imaging sensors, no SPM-based technique exists for probing the local pyroelectric response on a nanometre scale.

Soft pyroelectric materials based on the semicrystalline polymer poly(vinylidene fluoride) (PVDF) are investigated intensively with regard to large-area and low-cost applications such as IR sensing and thermal imaging,[3] microcalorimetry,[4] nonvolatile memories[5,6] and, recently, optothermal sensors integrated with organic thin-film transistors.[7] Ultrathin PVDF films have been the base material to prove the existence of two-dimensional ferroelectricity.[8] Due to their rather complex structure (ferroelectric crystallites embedded in an amorphous matrix) the pyroelectric response in such films is strongly determined by local variations in crystallinity, crystallite orientation, phase content, domain structure, and poling history.[9] For improving the overall pyroelectric activity and in order to allow for a sustainable tuning of material properties[10,11] it is essential to determine the local distribution of the pyroelectric coefficient with sufficiently high resolution.

Years ago it has been shown that fluoropolymer piezoelectric thin films can be locally poled in micron-sized areas by using conductive atomic force microscopy (AFM).[12] Recent piezoresponse force microscopy studies of the ferroelectric copolymer poly(vinylidene trifluoroethylene) [P(VDF-TrFE)] demonstrated sophisticated techniques for the alignment of lamellar crystallites,[13] the creation of ferroelectric domains as small as 30 nm,[14] and independent switching of the polarization direction of neighboring grains.[15] In addition, the spontaneous polarization has been manipulated at the nanometre scale in order to influence the surface reactivity[16] and to control the charge distributions in carbon nanotube field-effect transistors.[17] In none of these activities it has been attempted to investigate the pyroelectric effect locally.

Our scanning probe microscopy method—we abbreviate it pyroelectric scanning probe microscopy (PyroSPM)—is based on a local detection of the pyroelectric-related change in polarization via scanning surface potential microscopy (SSPM). SSPM maps the electrostatic potential on the sample's surface by applying a voltage to the tip that nullifies the force experienced between tip and sample. The pyroelectric effect results from periodic heat changes that are macroscopically induced by a laser beam. Therefore the conditions of the laser focus and its beam profile are of minor importance for the accuracy of the method. This is in contrast to conventional pyroelectric scanning microscopy methods where the heating is done locally by scanning a focused laser spot over the top electrode of a pyroelectric capacitor while measuring the pyroelectric current macroscopically.[18] With the PyroSPM method, the activation as well as the detection of the pyroelectric response can be done directly (without top electrode) on a nanometre scale. The potential of PyroSPM is demonstrated on the basis of P(VDF-TrFE) thin films. Here we show that a high-resolution map of the pyroelectric coefficient can be generated, paving the way toward a depth-sensitive characterization of materials with a nonuniform distribution of ferroelectric phases.

II. MEASUREMENT PRINCIPLE

Pyroelectricity is the electrical response of a material to a change in temperature and is correlated with the amount of aligned molecular dipoles. The pyroelectric coefficient p_{pyro} describes the connection between the change in temperature ΔT and the change in the electric displacement D and, in the absence of external electric fields, is given by the tempera-

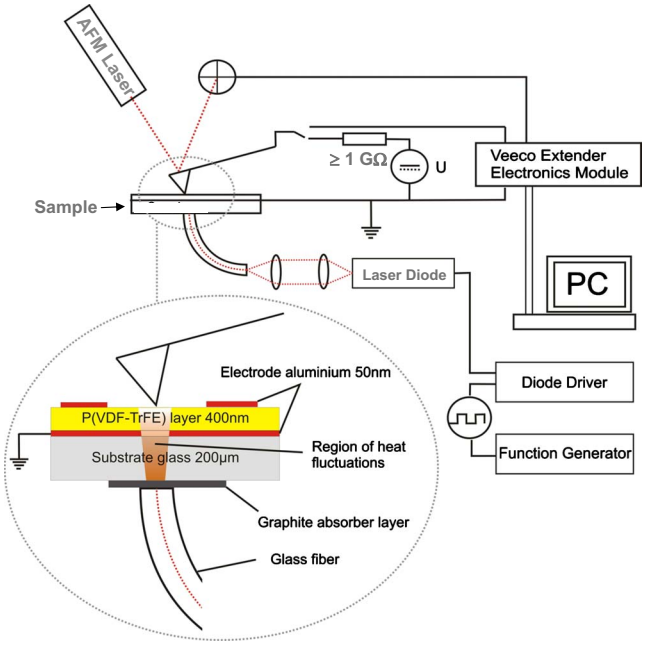

FIG. 1. (Color online) Setup of the PyroSPM method including a detailed view of the sample indicating the region of heat fluctuations.

ture variation in the macroscopic spontaneous polarization P_S

$$p_{\text{pyro}} = \frac{\Delta D}{\Delta T} = \frac{\Delta P_S}{\Delta T}. \tag{1}$$

The measurement principle of the PyroSPM method comprises a two step process (see Fig. 1). In the first step a potential larger than the coercive field of the ferroelectric crystallites in the polymer is applied to the tip thus orienting the dipoles vertically to the sample surface. This is done in contact mode in a small area of the sample and is termed "poling." The alignment of the dipoles is expected to result in a macroscopic spontaneous polarization accompanied by an increased surface charge density, which, in a subsequent scan, is detected as an increased surface potential around the poled region. Overall, the poling step defines a sample volume where the crystalline dipoles are aligned preferentially perpendicular to the sample surface with upward or downward pointing polarization depending on the direction of the applied poling field.

In the second step the pyroelectric readout is performed by probing the surface potential simultaneously with the temperature switching. To introduce different temperature states in the sample, light from an infrared laser diode (808 nm) is coupled to the sample from the backside via a glass fiber (Fig. 1). The laser intensity is periodically switched on and off thus forcing the temperature of the pyroelectric sample to oscillate between two equilibrium values. Depending on the polarization direction which has previously been defined in the poling step, charges are generated and the surface potential changes periodically according to the temperature modulation. More details on the measurement setup and principle are given in the Appendix D.

If the value of the temperature change ΔT is known the pyroelectric coefficient can be extracted from the PyroSPM measurement. The temperature induced change in the spontaneous polarization is measured as a surface potential change ΔV_{tip} at the AFM tip and p_{pyro} is calculated according to

$$p_{\text{pyro}} = \frac{1}{\Delta T}\frac{\Delta V_{tip}}{d}\varepsilon_0\varepsilon_{\text{pyro}}. \tag{2}$$

Here, $\varepsilon_{\text{pyro}}$ is the dielectric constant of the pyroelectric layer and d is the thickness of the layer portion with aligned ferroelectric crystallites.

III. RESULTS

In Fig. 2(b) surface potential scans from a 385-nm-thick P(VDF-TrFE) copolymer thin film with 65:35% of VDF:TrFE are performed 3 min after poling at −100 V (upper spot) and +100 V (lower spot). Details of the sample preparation are given in the Appendix D. In the simultaneously recorded height measurements [Fig. 2(a)] no influence of the poling on the surface morphology is detected. The poling voltage is applied on each spot over a time period of 20 s; negatively poled regions appear dark, whereas positively poled regions are bright in SSPM.

A scan profile taken along the black line indicated in Fig. 2(b) reveals that the poling results in the formation of 5 $\times 5$ μm^2 regions with a negative surface potential for negative poling voltages and a positive potential for positive poling [black curve in Fig. 2(d)]. The potential maxima are ± 1.0 V. These values are quite high and are due to an optimized poling procedure resulting in a strong spontaneous polarization. The sizes of the poled spots strongly depend on the poling time, ranging from 400 nm^2 for a poling time of 0.05 s to 5 μm^2 for poling over 20 s. If the surface potential is identified with a macroscopic spontaneous polarization then negative poling generates out-of-plane directed polarization and positive poling induces into-the-plane directed polarization.

Next the readout of the pyroelectric response to the laser-induced temperature modulation is performed within a time period of about 6 min after the poling. The AFM is set to perform the topography and surface potential scan within one second. The laser is driven with a square function of 0.1 Hz hence changing the temperature environment in the sample every five seconds. In Fig. 2(c) a surface potential scan across the two inversely poled regions is shown that is recorded simultaneously with the laser excitation. The temperature-induced changes in the spontaneous polarization appear as stripes and are visible only in the poled domains. One stripe corresponds to five scan lines, which requires approximately five seconds. As is deduced from the section profile taken along the red line indicated in Fig. 2(c), the temperature-induced potential fluctuations are strongest in the center of the poled regions [red–thick line curve in Fig. 2(d)]. The inset of Fig. 2(d) displays the shape of the potential variations in detail. The square wave form of the temperature enhancement obviously translates into the voltage response of an RC component (resistor-capacitor compo-

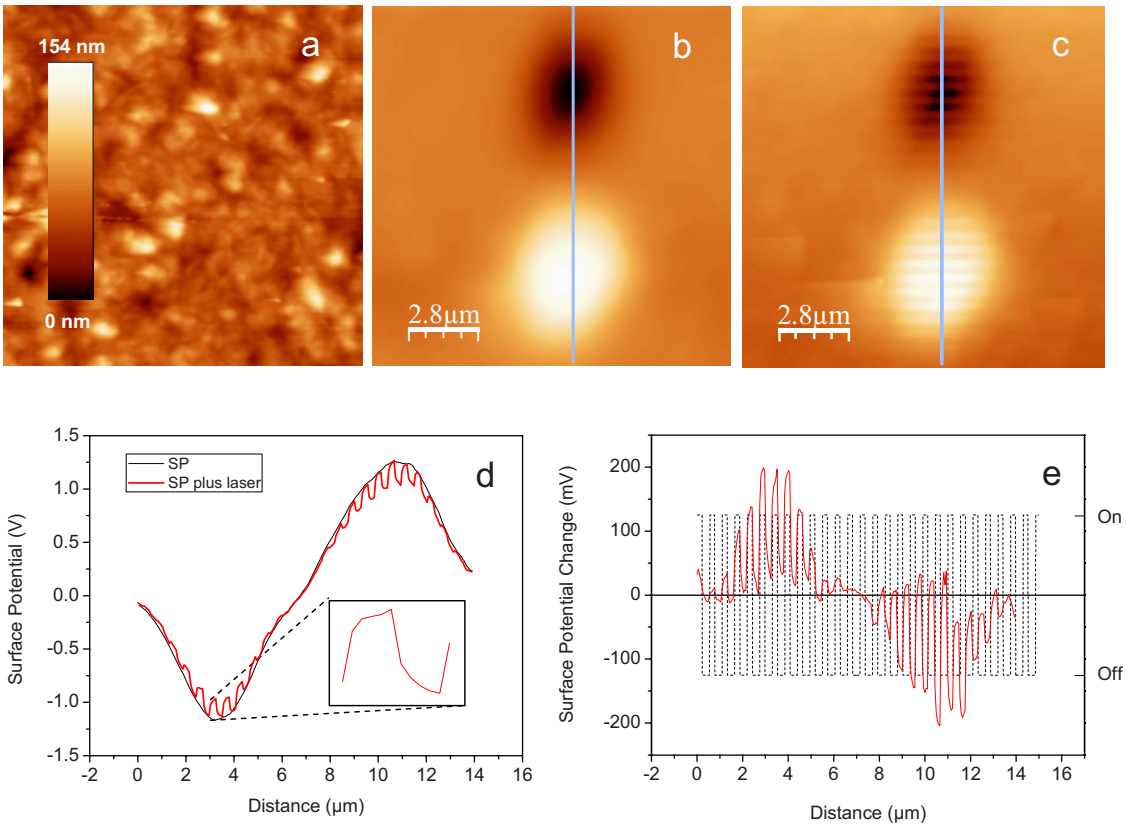

FIG. 2. (Color online) (a) AFM topography image of a 65:35% P(VDF-TrFE) thin film recorded simultaneously with the surface potential. (b) Surface potential scan (256×256 lines) indicating two regions that were inversely poled. The dark region results from negative poling at V_P=−100 V and corresponds to a macroscopic polarization pointing out of the plane, the bright region results from positive poling at V_P=+100 V and corresponds to a macroscopic polarization pointing into the plane. (c) Variations in the surface potential by periodic laser excitation (0.1 Hz): the surface potential changes appear only in the poled regions (brighter stripes in the dark negatively poled region and darker stripes in the bright positively poled region). (d) Profile of the surface potential taken across the lines indicated in (b) and (c). The inset is a closeup of the potential fluctuations induced during one cycle. (e) Change in the surface potential during laser excitation along the line displayed in (c). The pyroelectric response is strongest in the center of the spots. The simultaneous variation of the laser intensity between on state and off state is also shown, which indicates the inverse response of regions with opposite polarization direction.

nent). Such a time dependence is typically observed in the voltage response of macroscopic capacitive pyroelectric sensors.[19,20] Subtracting the black from the red curve in Fig. 2(d) visualizes the surface potential changes more clearly [Fig. 2(e)]. The sign of the changes is opposite for the oppositely poled regions, the maximum amplitude of the fluctuations is about −200 mV in the positively and +200 mV in the negatively poled spots. In Fig. 2(e) the variation in the laser intensity over the scanned region is also displayed. In the negatively poled region where the polarization direction points into-the-plane the switched-on laser induces a positive surface potential change whereas it induces a negative change in the positively poled region with out-of-plane pointing polarization direction. This means that a temperature enhancement induces a decrease in the absolute surface potential value and therefore a decrease in the spontaneous polarization. Such a behavior is expected for materials with a negative pyroelectric coefficient.[2]

For generating a map of the pyroelectric coefficient according to Eq. (2) two parameters have to be known: one is the layer thickness of the sample portion contributing to the spontaneous polarization d and the other one is the temperature enhancement ΔT induced by the laser.

The former is associated with the penetration depth of the coercive electric field induced by the tip and can be calculated by the method of mirror charges (see Appendix A, Figs. 6 and 7). For a poling voltage of 80 V the layer thickness of the sample portion with aligned crystallites is about d =120 nm.

The temperature enhancement ΔT has to be calculated by solving the one-dimensional thermal diffusion equation for a multilayer system composed of a 175-μm-thick glass substrate, a 400-nm-thick P(VDF-TrFE) layer and electrodes of 50 nm layer thickness. A special feature of the PyroSPM method is the laser induced excitation of the temperature changes from the sample's backside via the substrate. Details of the modeling are described in the Appendix B (Figs. 8 and 9) and in Ref. 23.

In Fig. 3 the frequency dependence of the calculated ΔT in the pyroelectric layer for varying thickness values of the glass substrate is shown assuming an excitation laser power of 0.8 W/cm^2. The induced temperature change ΔT de-

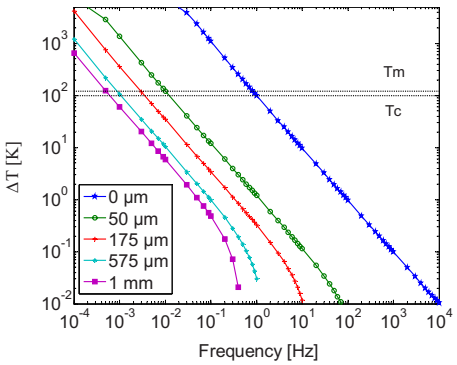

FIG. 3. (Color online) Temperature enhancement ΔT in the pyroelectric layer depending on the frequency of the heat fluctuations and the substrate layer thickness. The parameters assumed for the calculation are a pyroelectric layer thickness of 400 nm and an electrode layer thickness of 50 nm. The melting temperature (T_m) as well as the Curie temperature (T_c) are indicated in the graph. They correspond to a P(VDF:TrFE) composition of 76:24 mol %.

creases with increasing thickness of the substrate indicating that the latter acts as a heat sink. The decrease with frequency is due to the decreasing penetration depth of the heat waves in the pyroelectric layer. In Fig. 3 two horizontal lines are also drawn, which are the melting temperature (T_m) and the Curie temperature (T_c), the latter indicating the ferroelectric-paraelectric phase transition. They indicate the limit of validity of the model; for higher temperatures the ferroelectric properties of the pyroelectric layer will disappear. At a modulation frequency of 0.1 Hz the calculation yields $\Delta T \sim 3$ K for a glass substrate thickness of 175 μm (Fig. 3). The correctness of the model has also been validated by simulating and measuring the macroscopic pyroelectric response of capacitors fabricated on an identical substrate (see Appendix B, Fig. 9). The correlation between calculation and measurement of the macroscopic pyroelectric current and voltage response for backside exposure is excellent, thus confirming the calculated ΔT values. The pyroelectric coefficient used for the modeling is 30 $\mu C/Km^2$. Therefore the macroscopic pyroelectric characterization can be used to calibrate the microscopic one. Moreover, for heterogeneous materials with unknown parameters (thermal conductivity, specific heat, etc.) the comparison with the macroscopic response measurement can be utilized to extract these quantities.

IV. EVALUATION

For the generation of a microscopic map of the pyroelectric coefficient the temperature-induced change in the spontaneous polarization at each point of the sample has to be recorded via a high-resolution scan of 512×512 points. The temperature is varied by switching the laser on and off every 5 s. The corresponding surface potential modulations measured with the PyroSPM setup are used to create the two-dimensional distribution of the pyroelectric coefficient by taking the highest potential difference of four subsequently scanned lines, thus resulting in a map with one-fourth of the resolution in the direction perpendicular to the scan direction (128×512 points). Clearly, the resolution of the map is influenced by the sharpness of the tip, field spreading from the tip and field contributions of the tip cone and the cantilever thus summing up to a lower resolution limit of about 50–100 nm. However, it is also determined by the number of image points and the fine structure of the poled regions which depends on the grain size and the poling voltage. Since the fluoropolymer grain size is about 200 nm it is the morphology that mainly determines the resolution for densely scanned surfaces.

In order to demonstrate this procedure we defined a pattern of pyroelectric active regions. This was done via sequential positive poling of spots forming the shape of a "J" and sequential negative poling of spots forming the shape of an "R" thereby creating a pattern of the institution's logo (Fig. 4). As probing material a ferroelectric P(VDF-TrFE) copolymer layer (76:24) with a thickness of 340 nm was used.

In Fig. 4(a) the topography of the sample is depicted as derived from AFM height measurements. The ferroelectric crystallites appear as spaghettilike structures surrounded by a cloudy amorphous matrix. The poling was performed with a voltage of $V_p = \pm 80$ V applied over a period of 4s for each spot. Figure 4(b) shows the surface potential scans done approximately 60 min after poling—a clear rise in potential is seen. The bright region belongs to the positively poled J and the dark one to the negatively poled R but the pattern appears very smeared out which is mainly due to the time period elapsed after poling. The maxima of the surface potential resulting from the induced surface charges are ± 200 mV which is smaller than in Fig. 2(b). Reasons for that are a reduction of poling voltage and poling time and a larger time period between poling and measurement. As discussed in the Appendix A (Fig. 7), the surface potential decreases with time which is due to a gradual redistribution of the surface charges to the interfaces between crystallites and amorphous phase in the bulk. These charges locally compensate the high depolarization fields thus stabilizing the crystalline polarization. The hierarchy of the time scales for scanning, laser excitation, and potential decay are 1 s to scan one line, 10 s is the periodic time of the laser excitation and on the order of hours for a complete screening of the induced surface potential.

Next the pyroelectric effect was activated by switching on the laser modulation with an intensity of 2.7 mW/mm^2. In Fig. 4(c) the temperature induced surface potential changes appear as dark stripes in the positively poled J areas (2 μm^2) and as bright stripes in the negatively poled R ones (1 μm^2). From ΔV_{tip} the values for the pyroelectric coefficients were extracted according to Eq. (2) by using $\Delta T = 3$ K, a dielectric constant $\varepsilon_{pyro} = 13.5$ and a maximum poling penetration depth of $d = 120$ nm. In Fig. 4(f) a map of p_{pyro} is plotted. In the positively as well as negatively poled regions the maximum values of p_{pyro} are found in the center of the poled spots achieving values up to 40 $\mu C/m^2/K$ and 25 $\mu C/m^2/K$, respectively. Because of the sensitivity of the method to the poled layer thickness in-depth profiling of the polarization and of the crystalline phase distribution is conceivable.

In order to test the stability of the pyroelectric activity the same type of measurements is repeated 20 h after poling by leaving the sample overnight [Figs. 4(d), 4(e), and 4(g)].

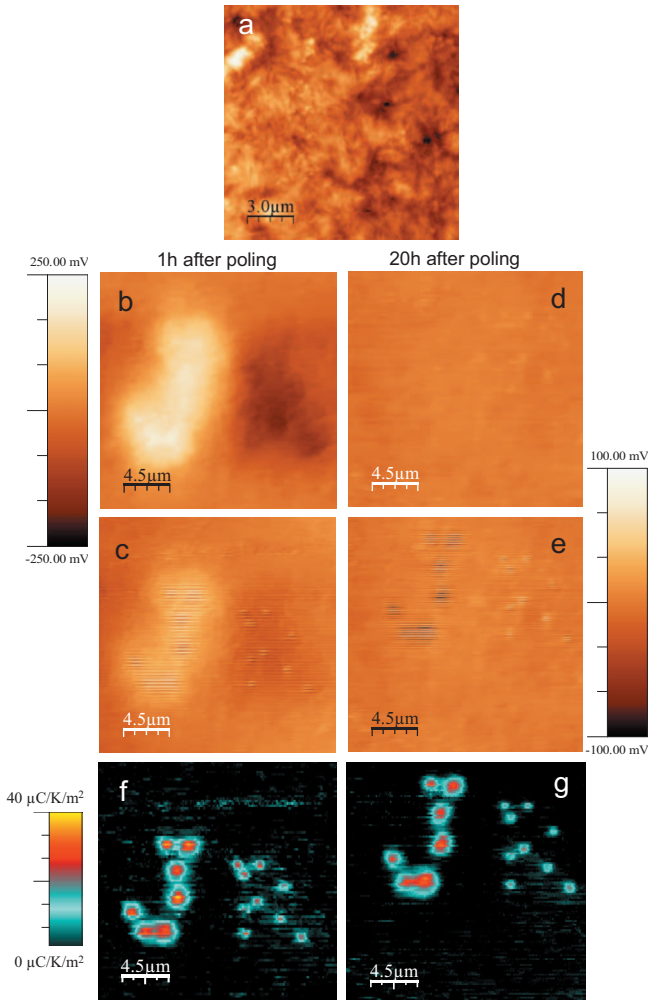

FIG. 4. (Color) Fabrication of a pyroelectric active JR pattern of positively (J) and negatively (R) poled regions in P(VDF-TrFE) layers. (a) Topography of P(VDF-TrFE) with 24 mol % TrFE, (b) surface potential scan of the copolymer after poling, (c) surface potential scan of the copolymer during laser excitation, (d) surface potential scan of the copolymer 20 h after poling, (e) surface potential scan of the copolymer during laser excitation 20 h after poling, (f) map of the pyroelectric coefficient of the copolymer for $\Delta T=3$ K, and (g) map of the pyroelectric coefficient of the copolymer 20 h after poling.

Without laser excitation no clear structure in the surface potential is observable, only few traces of positive screening charges at the negatively poled spots survived [Fig. 4(d)]. As expected, the surface charges are redistributed in the bulk and trapped at the interfaces between crystalline and amorphous phase. Nevertheless, during excitation the inscribed polarized structures clearly appear as dark striped spots in the positively poled region and bright striped spots in the negatively poled region [Fig. 4(e)]. The pyroelectric coefficient [Fig. 4(g)] slightly decreased for the positively poled spots but remained absolutely constant for the negatively ones. In Fig. 5 the lateral distribution of p_{pyro} across one positively poled spot and its time dependence are displayed. A 20% decrease in p_{pyro} is observed; after one day a maximum value of 34 $\mu\mathrm{C}/\mathrm{m}^2/\mathrm{K}$ is measured [Fig. 5(b)]. A similar value for p_{pyro} was deduced from macroscopic measurements (compare SI Fig. 4).

These observations are consistent with the hypothesis that most of the signal recorded in the surface potential mode directly after poling is due to excess charges. After redistribution of these charges to the interfaces the regions with significant remnant polarization clearly appear when excited by a periodic heat flow. Then, due to the pyroelectric effect resulting in a periodic decrease in the spontaneous polarization, excessive compensation charges are released from their traps at the interfaces and appear as modulations of the surface charge. The modulations directly translate into a pyroelectric coefficient originating from the aligned ferroelectric crystallites. The strong depolarization fields that are a consequence of the inhomogeneous poling induce a gradual retention of the spontaneous polarization. For the negatively poled spots (R region) this retention is stronger and occurs on a shorter time scale, resulting in a higher value for the pyroelectric coefficient in the J region. Differences in the loss of polarization between oppositely poled domains have previously been attributed to the asymmetry of boundary conditions in the tip/film/electrode heterostructure, resulting in different depolarization fields.[21] In a similar experiment performed on paraelectric PVDF no appreciable pyroelectric activity was detected (see Appendix C, Fig. 10).

V. SUMMARY

The present work demonstrates a surface scanning method for the quantitative determination of the local pyroelectric coefficient in ferroelectric thin films. It is called pyroelectric scanning probe microscopy and allows generating a map of the pyroelectric response with very high spatial resolution. PyroSPM can overcome previously existing limitations in resolution of conventional scanning pyroelectric microscopy methods. The method is based on the surface potential mode of a standard AFM, which additionally has to be equipped with a temperature modulation unit. By applying a sufficiently high voltage to the conductive tip (in contact mode AFM) a preferential orientation of the polarization in the ferroelectric crystallites is achieved locally. In the as-poled samples small heat fluctuations were achieved by laser diode excitation from the bottom side thus inducing changes in the surface potential due to the pyroelectric effect. These surface potential variations were detected simultaneously and used to extract an electrode-free map of the pyroelectric coefficient. The potential of the method is demonstrated on the basis of ferroelectric semicrystalline P(VDF-TrFE) copolymer thin films. For high scanning rates the resolution is determined by the size of the ferroelectric crystallites. The detection of temperature changes down to 0.5 K is in the realm of possibility. The method enables in-depth profiling of the polarization and visualization of internally screened regions as a function of excitation frequency. Therefore PyroSPM provides possibilities to study the composition dependence and dynamics of ferroelectric nanodomains.

ACKNOWLEDGMENTS

The Austrian Forschungsförderungsgesellschaft (FFG) is

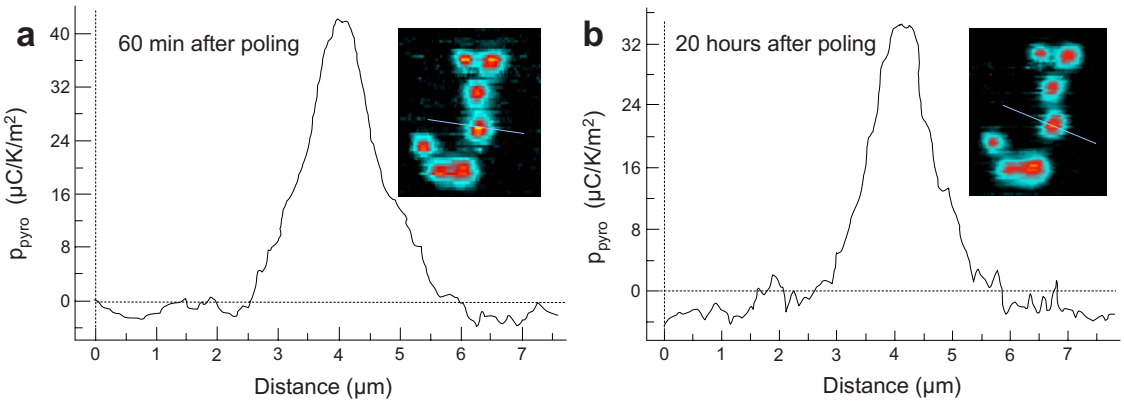

FIG. 5. (Color online) (a) Scan across the middle spot of the J pyroelectric coefficient (see inset). (b) Same, 20 h after poling.

gratefully acknowledged for supporting this work via funding under Project No. 808.004 (Integrated organic sensors). We also thank Siegfried Bauer from the Johannes-Kepler-University in Linz for many fruitful discussions.

APPENDIX A

To get an estimation of the potential induced in the sample by local poling, the field distribution between tip and sample is modeled by means of the method of mirror charges, a standard problem in electrostatics.[22] The starting point of the potential modeling forms the Poisson equation; it has to be solved for the following configuration: a pointlike potential source (tip) in front of two dielectrics (air +PVDF) and a conductive plane (bottom electrode). Details of the calculation can be found in Refs. 22 and 23.

In Fig. 6(a) the calculated spatial distribution of the z direction of the electric field (E_z) induced by an 80 V constant potential (applied to the tip) is plotted over the cross section of the pyroelectric layer. The tip is located at 400 nm lateral position. The field distribution in the sample is by no means homogeneous. The ellipsoidal equipotential plane corresponding to a field of $E_P=10$ MV/m (dark red) extends to the bottom electrode, whereas the planes for $E_P=20$ MV/m (light red), $E_P=60$ MV/m (yellow), and for $E_P=100$ MV/m (white) have decreased penetration depths. Once the coercive field is reached the dipoles in the corresponding penetration volume are fully aligned, thereby raising the potential difference to the largest possible value (per unit layer thickness). From hysteresis measurements on macroscopic P(VDF-TrFE)-based capacitors we know that the coercive field strength is about 60 MV/m, which for a poling voltage of 80 V, is reached only within a depth of 120 nm from the surface according to the calculation. The poled region is illustrated in the right part of Fig. 6(b) as the region within the yellow balloon. Here the structure of the semicrystalline PVDF-based copolymer is sketched, illustrating

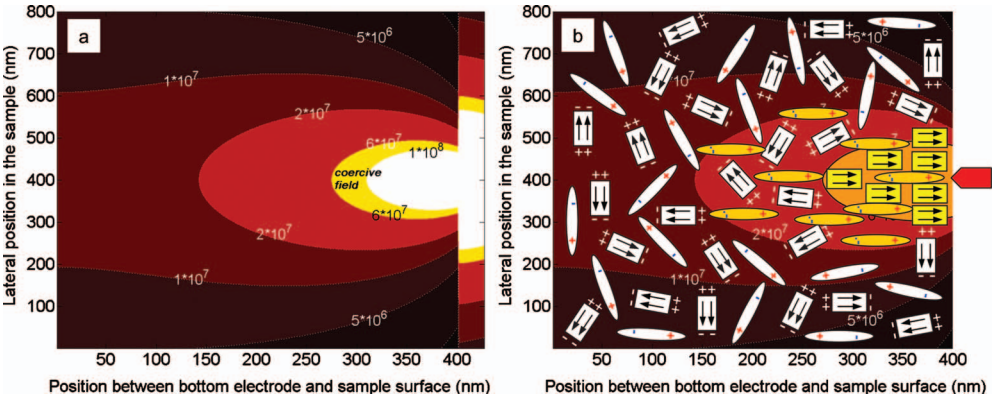

FIG. 6. (Color) (a) Vertical component of the electric field induced by a pointlike tip located at 400 nm lateral position and 10 nm distance to the surface for a voltage of +80 V applied between tip and sample bottom ($\varepsilon_{PVDF}=13.5$, $\varepsilon_{air}=1$). The sample surface is located 400 nm away from the bottom. The numbers indicted are the potential values associated with the different equipotential lines, given in MV/m (b) Scheme of the local distribution of polarization in a semi-crystalline fluoropolymer under the influence of a tip-induced external electric field as calculated in (a). The ferroelectric polarization is represented by rectangles whereas the dipoles of the amorphous phase appear as ellipses. At the interface between crystalline and amorphous phase charges are trapped which compensate for the strong depolarization fields, thereby stabilizing the ferroelectric polarization. In addition, there are also excess charges accumulated at the interface (Maxwell-Wagner effect). Within the yellow balloon ($E_P>6\times10^7$ V/m) the dipole vectors of the crystallites as well as the dipoles from the amorphous phase are aligned parallel to the external electric field direction (here the interface charges are not drawn). Within the light-red balloon ($E_P>2\times10^7$ V/m) only the amorphous dipoles are aligned.

the dipoles of the ferroelectric crystallites (rectangles) as well as the molecular dipoles from the amorphous phase (ellipses). In addition, charges at the interface between amorphous and crystalline regions have to be taken into account (Maxwell-Wagner interface charges,[9]). Within the yellow balloon all dipoles (crystalline, amorphous, and interface) are aligned parallel to the external electric field, giving rise to a predominantly crystalline polarization. In the volume of the sample, where the field is below the coercive threshold, no preferential orientation of crystallite dipoles is generated. Within the light-red balloon only the dipoles of the amorphous phase and the excess charges at the interface are aligned resulting in a small amorphous and interface polarization. Here the electric field is below the coercive field of the crystalline phase. However, it is known that the small contribution of the amorphous phase and of the interface ($<10\%$) to the overall polarization is not very stable.[9]

Therefore it has to be assumed that the alignment of the crystallite dipole moments leading to a macroscopic polarization is achieved only in the sample volume within the yellow balloon [see Fig. 6(b)]. When the potential at the tip is further increased, the coercive field, which is necessary for the alignment of the dipoles, is reached in a larger volume of the sample resulting in a further increased spontaneous polarization. Consequently, for increasing poling voltage the volume of the aligned region expands due to the increasing penetration depth of the coercive field and the increasing lateral extension of the corresponding equipotential plane. The penetration depth of the coercive vertical electric field is about 170 nm for $V_P=100$ V as compared to 120 nm for $V_P=80$ V. The maximum surface potential enhancement also increases with the poling voltage; however, there exists an upper limit of about $V_P=100$ V which should not be exceeded to avoid irreversible degradation of near-surface regions right below the tip.

Increasing the poling time has a similar effect on the poling volume; here it is mainly the lateral growth of domains and the creation of a lot of excess charges at the interface between amorphous and crystalline phases that enlarges the volume of the region with aligned dipoles.

It is worth mentioning that the poling induced surface potential is not stable in time; in fact it exhibits an exponential decay [see Fig. 7(b)] caused by a fast decrease in the induced surface charge density. For a better understanding of this effect one has to account for the semicrystalline nature of the P(VDF-TrFE) material. The poling induced surface charges are partly used to stabilize the polarization of the crystallites and the amorphous dipoles[23] and partly accumulate as excess charges at the amorphous-crystalline interface resulting in an interface polarization (Maxwell-Wagner interface polarization).[9] After removal of the external poling field the surface charges quickly redistribute throughout the sample volume where they locally compensate the strong depolarization fields and therefore stabilize the crystalline macroscopic polarization.

Effects of surface potential screening by the adhesion of charged particles from the atmosphere as described in Ref. 24 are not observed. Nevertheless, it is also conceivable that a relaxation of the dipole alignment occurs with time due to high depolarization fields resulting from a nonuniform polarization distribution throughout the sample volume.

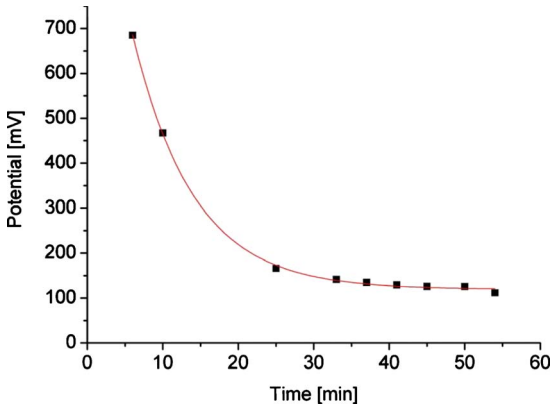

FIG. 7. (Color online) Decay of the surface potential after poling with +80 V. The time dependency is described by an exponential function.

APPENDIX B

In general, the pyroelectricity of a region depends on the amount of molecular dipoles orientated in the same direction and therefore leading to a spontaneous macroscopic polarization $\vec{P}_s$.

$$\vec{P}_s = \frac{1}{V}\sum \vec{P}_i, \tag{B1}$$

where $\vec{P}_i$ is the molecular dipole moment and V the volume of the sample.

The pyroelectric coefficient describes the connection between the change in temperature and the change in the electric displacement $\vec{D}$

$$\vec{\mathbf{p}}_{\mathbf{pyro}} = \frac{d\vec{D}}{dT} = \frac{d}{dT}(\varepsilon\vec{E} + \vec{P}) = \frac{d\vec{\mathbf{P}}_s}{dT}. \tag{B2}$$

For materials with temperature-independent permittivity ε the thermal variation in the electric displacement is determined by the thermal variations in the spontaneous and the dielectric polarization $P=P_E+P_S$, where $P_E=\chi E$ accounts for the polarizability of the material in the presence of an electric field and P_S arises from the alignment of the dipoles. In the case under consideration the single contribution to the change in D arises from the change in P_S since no external field is applied and the polarizability remains constant.

When exact values of the temperature change are available the pyroelectric coefficient can be extracted from the PyroFM measurement. In this regard the temperature change induced by the laser modulation is calculated from a heat conduction model for a multilayer system such as the one displayed in Fig. 8. It is composed of a 175-μm-thick glass substrate, a 400-nm-thick P(VDF-TrFE) layer and aluminum electrodes of 50 nm thickness.

Following the approach of Appendix D. Setiadi and Regtien[25] one has to resolve the one-dimensional thermal diffusion equation as described in Ref. 23

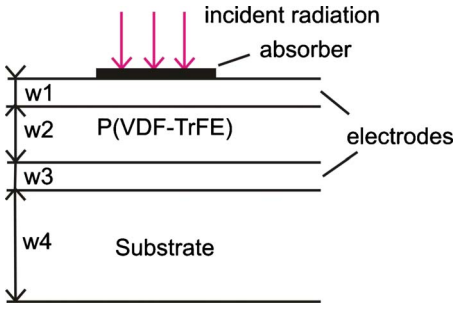

FIG. 8. (Color online) Layer setup of the modeled samples

$$\frac{\partial T(x,t)}{\partial t} = \frac{\delta_n}{c_n d_n} \frac{\partial^2 T(x,t)}{\partial x^2}. \tag{B3}$$

The material properties δ_n, c_n, and d_n for each layer are given in Table I.

For a periodic heat excitation with frequency ω and the use of equation

$$T_n(x,t) = T_n(x) e^{j\omega t} \tag{B4}$$

it is possible to separate the time and space variables. Then the problem is reduced to solve the time independent equation:

$$T_n(x) = \frac{\delta_n}{j\omega c_n d_n} \cdot \frac{\partial^2 T_n(x)}{\partial x^2}. \tag{B5}$$

The general solution of this equation for each of the n layers is

$$T_n(x) = A_n e^{\alpha_n (x-h_n)} + B_n e^{-\alpha_n (x-h_n)} \tag{B6}$$

with

$$\alpha_n = \sqrt{\frac{j\omega c_n d_n}{\delta_n}}. \tag{B7}$$

The coefficients A_n and B_n have to be determined by the boundary conditions, respectively. h_n is defined as $h_n = \Sigma_1^n w_{n=1}$ with w_n being the thickness of the nth layer. As a second equation the spatial heat current density J of each layer has to be taken which is defined as

$$J_n(x) = -\delta_n \cdot \frac{\partial T_n(x)}{\partial x}. \tag{B8}$$

In Eq. (B8) δ_n is the heat conductivity of the nth layer. The problem can now be solved analytically with the help of boundary conditions at each layer. For the front side of the sensor element the boundary condition is expressed as.

TABLE I. Material properties.

Material	Heat Conductivity (W K^{-1} m^{-1})	Specific Heat (J K^{-1} kg^{-1})	Density (kg m^{-3})
Al	237	896	2707
P(VDF-TrFE)	0.1287	1233	1880
Glass	1	670	2500

$$J_1(0) = \eta \cdot P_1 - g_H T_1(0). \tag{B9}$$

In Eq. (B9) P_1 is the incoming radiation from the laser and η is the absorption coefficient while g_H is the heat radiation transfer coefficient accounting for the heat loss per unit area at the front and at the back side of the sensor. For an n-layer system the boundary condition at the back side is given by

$$J_n(w_n) = g_H T_n(w_n). \tag{B10}$$

The boundary conditions for the interfaces between two adjacent layers can be derived from the continuity of the temperature and the heat current density

$$T_n(w_n) = T_{n+1}(h_{n+1}),$$

$$J_n(w_n) = J_{n+1}(h_{n+1}). \tag{B11}$$

By substituting Eqs. (B6) and (B8) into the expressions for the boundary conditions in Eqs. (B9)–(B11) a system of linear equations is generated that is enough to find a solution for the complex coefficients A_n and B_n as a function of frequency.[23]

In principle, this analysis is focused on the calculation of the average temperature in the pyroelectric layer, which in our model is the second layer for laser excitation from the top and the third layer for excitation from the bottom side. In the latter case the labels have to be assigned differently with the substrate being the first layer, the bottom electrode the second and so on. For bottom excitation, as it is relevant for PyroSPM, the average temperature of the pyroelectric layer with the thickness w_3 is expressed as

$$\bar{T}(t) = \frac{1}{w_3} \int_0^{w_3} T_3(x,t) dx \tag{B12}$$

with

$$\bar{T}(t) = \frac{\eta P_1}{\alpha_3 w_3} [a_3 (e^{\alpha_3 w_3} - 1)] + b_3 (1 - e^{-\alpha_3 w_3}). \tag{B13}$$

In Eq. (B13) P_1 is the power of the exciting laser light whereas a_3 and b_3 are coefficients defined by $a_3 = A_3 / \eta P_1$ and $b_3 = B_3 / \eta P_1$. The influence of the layer properties on the thermal behavior of the pyroelectric capacitor is included in these coefficients.

For harmonic laser excitation the time-dependent part of the average temperature enhancement can be written as

$$\bar{T}(t) = \bar{T}(\omega) e^{i\omega t} \tag{B14}$$

Due to thermal diffusion and the boundary conditions the temperature change in the pyroelectric layer is not only determined by the properties of the pyroelectric layer itself but also by the material and the thickness of the substrate. A temperature variation in the pyroelectric layer that is induced by a modulated infrared radiation results in an electric output signal.

The frequency-dependent current and voltage response functions are then deduced from the temperature enhancement according to

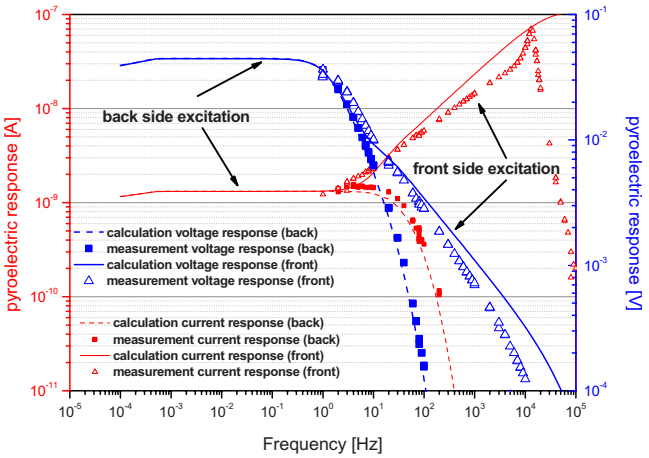

FIG. 9. (Color online) Measured and calculated pyroelectric current (red or small symbols–thin lines) and voltage (blue or large symbols–thick lines) response of a macroscopic P(VDF-TrFE) capacitance sample with 24% TrFE. The measurement setup for front side excitation is equivalent to the one in Fig. 1 with the exception that the response is extracted via the top electrodes. The calculations for backside exposure were done for a pyroelectric layer thickness of 285 nm and by assuming laser excitation from the back and in-coupling of the laser by means of a glass fiber. The thickness of the glass substrate is 175 μm.

$$I = p_{\text{pyro}} A \cdot \frac{\partial \bar{T}}{\partial t} = p_{\text{pyro}} A \omega \cdot \bar{T} = p_{\text{pyro}} A \omega \cdot \Delta T,$$

$$V = I \frac{R}{\sqrt{1 + \omega^2 R^2 C^2}}. \quad \text{(B15)}$$

Here R is the resistance and C the capacitance of the overall equivalent circuit, and A is the area of the pyroelectric capacitor.

In Fig. 9 experimental results from macroscopic pyroelectric measurements of the voltage and the current response for top and bottom side excitation are compared to the calculations based on the described formalism. The parameters used for the calculations are the material properties given in Table I, the thickness values of the individual layers, the laser excitation power of 2.7 mW/mm^2, the independently determined absorption coefficient (0.9) and the pyroelectric coefficient (30 μC/K/m^2), which was measured separately as well. No fit parameters were used. The agreement between experiment and calculation is excellent, giving clear evidence for the applicability of the model and the accuracy of the calculated average temperature enhancement in the pyroelectric layer.

APPENDIX C

In order to investigate the sensitivity of the PyroFM method to nonferroelectric crystalline domains we repeated the experiment in Fig. 4 also for pure P(VDF), which is known to form predominantly the paraelectric phase when applied by spin-on. The results are summarized in Fig. 10. The topography of pure P(VDF) is more compact than of the copolymer layer without any sign of the spaghettilike ferroelectric crystallites [Fig. 10(a)]. Poling of spots forming the company's logo "JR" at $V_P = \pm 100$ V results in the appearance of a smeared out bright J in the positively poled region and a smeared out dark R in the negatively poled region in the surface potential scan taken 30 min after poling [Fig. 10(b)]. The poling induced change in the surface potential here is much smaller than it is for the copolymer sample (± 60 mV). Activation of the pyroelectric effect by switching on the laser results in very small modulations in the simultaneously recorded surface potential of the negatively poled spots [Fig. 10(c)]. No modulations are observed in the positively poled regions. Consequently, after extraction of the pyroelectric map according to Eq. (2) for a temperature increase of 3 K a small contribution to the pyroelectric activity is detected in the negatively poled R region with a maximum value for the coefficient of $p_{\text{pyro}} = 2$ μC/K/m^2

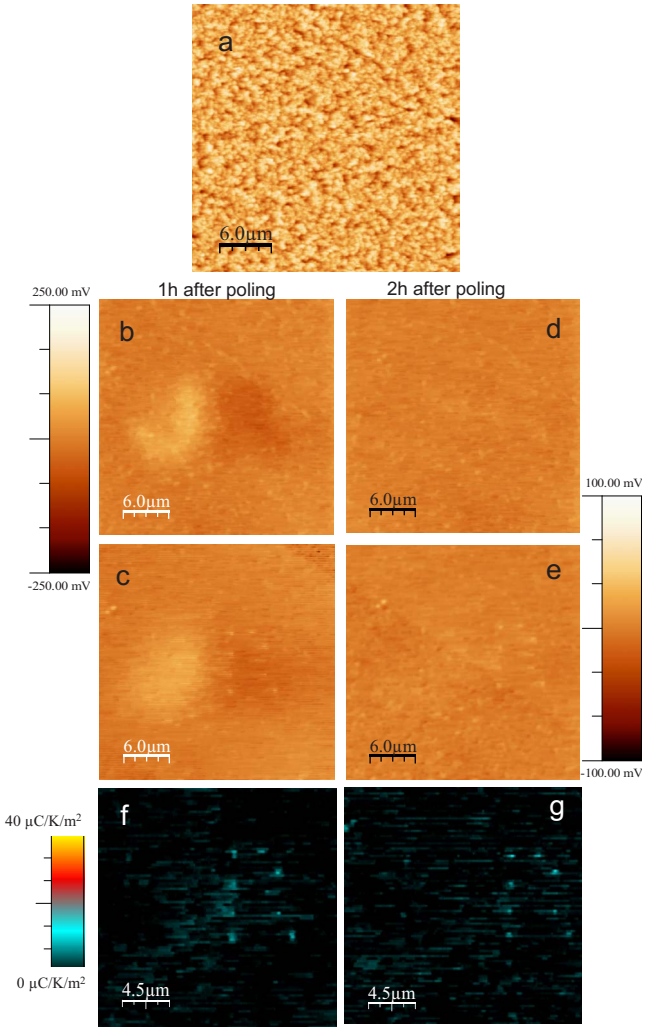

FIG. 10. (Color online) (a) Topography of pure P(VDF), (b) surface potential scan of the P(VDF) sample after positive poling of spots forming a J pattern and negative poling of spots forming an R pattern by applying $V_P = \pm 100$ V, (c) surface potential scan over the poled spots during laser excitation, (d) same, 2 h after poling, (e) same, during laser excitation 2 h after poling, (f) map of the pyroelectric coefficient of the pure P(VDF) for $\Delta T = 3$ K, and (g) two hours after poling.

[Fig. 10(f)]. This value is stable over several hours [Figs. 10(e) and 10(g)] and is attributed to the pyroelectric effect stemming from the metastable polarization of the amorphous phase. This is conceivable, since pure PVDF has a crystallinity of not more than 50%. The pyroelectricity of the amorphous phase accounts for about 5% of the overall pyroelectricity.[9] In the positively poled regions no pyroelectric activity is observed. The upward polarization of amorphous dipoles is obviously less stable than the downward polarization.

APPENDIX D

1. Material

The samples are composed of P(VDF-TrFE) thin films which are spin coated onto 50 nm sputtered aluminum bottom electrodes. For substrates 175-μm-thin glass slides are used. The samples are partially covered by aluminum top electrodes, they also serve as a reference area for the adjacent uncovered P(VDF-TrFE), where the macroscopic pyroelectric response is determined by the PyroFM method.

A P(VDF-TrFE) solution was produced by melting copolymer capsules in γ-butyrolactate solvent in a sol-gel procedure. Subsequently, thin films were created by spin coating at 1000 rps. Annealing of the samples for 5 h at a temperature of 383 K followed by slow cooling to room temperature over 10 h resulted in a strong presence of the ferroelectric β phase. In the β phase the all-trans structure is established and the dipoles in a molecule chain are orientated in the same direction. As source material, different mixtures of VDF and TrFE (VDF:TrFE=65:35,76:24,100:0, molar weight) are used, resulting in samples with varying degrees of crystallinity and different values of film thickness d ranging from 300 to 400 nm.[19] The thickness and optical constants of the dielectric layers are determined by ellipsometry based on a variable angle spectroscopic ellipsometer from J. A. Woolam Inc.

2. Surface potential measurement

The scanning surface potential measurement is done with a standard atomic force microscope (Veeco Dimension 3100) equipped with an extender electronics box which allows the separation of topographic and surface potential information employing a two-pass technique. In the first scan topographic and phase information are recorded and in the second scan the potential at the sample surface is detected using a Kelvin probe method, where the potential of the tip is adjusted to nullify the electrostatic interaction between tip and sample. We used an antimony coated silicon tip from Veeco with a resonant frequency around 68 kHz and a resistivity of less than 0.01 Ωm.

3. Poling

The poling of the ferroelectric domains of P(VDF-TrFE) copolymer thin films was done in AFM contact mode by applying a dc voltage V_P between tip and the sample's bottom electrode. The dc voltage was provided by an external source (Keithley 6487). If this voltage generates a field larger than the coercive field of the ferroelectric crystallites a preferential orientation of the crystalline dipoles will be induced that depends both on the strength as well as on the sign of the applied field. According to the thickness of the pyroelectric layer and the coercive field of the copolymer of about 60 MV/m poling voltages in the range of 70 $V \leq V_P \leq 100$ V were used in these experiments. The alignment of the dipoles is expected to result in a macroscopic spontaneous polarization accompanied by an increased surface charge density, which, in a subsequent scan, is detected as an increased surface potential around the poled region.

4. Pyroelectric readout

In order to introduce different temperature states in the sample, light from a focusable laser diode with 808 nm wavelength is coupled into a glass fiber having a diameter of 1000 μm (BFH48-1000 from Thorlabs) via standard optics (see Fig. 1). After out coupling, the infrared light is absorbed at the bottom side of the sample on an area defined by the diameter of the glass fiber (~ 1 mm^2). Optionally, the sample's bottom side is covered by a black graphite layer to improve absorption of the laser light. As the laser intensity is modulated by a square function between on and off by using a Keithley 6221 function generator, the temperature of the sample and the pyroelectric layer changes between two equilibrium states.

*barbara.stadlober@joanneum.at

[1] S. V. Kalinin and D. A. Bonnell, Phys. Rev. B **65**, 125408 (2002); for a review see *Nanoscale Characterization of Ferroelectric Materials*, edited by M. Alexe and A. Gruverman (Springer-Verlag, Berlin, New York, 2004).
[2] S. B. Lang, Phys. Today **58** (8), 31 (2005).
[3] S. Bauer, J. Appl. Phys. **80**, 5531 (1996).
[4] B. Neese, B. J. Chu, S.-G. Lu, Y. Wang, E. Furman, and Q. M. Zhang, Science **321**, 821 (2008).
[5] R. G. Naber, C. Tanase, P. W. M. Blom, G. H. Gelinck, A. W. Marsman, F. J. Touwslager, S. Setayesh, and D. M. de Leeuw, Nature Mater. **4**, 243 (2005).
[6] Z. Hu, M. Tian, B. Nysten, and A. M. Jonas, Nature Mater. **8**, 62 (2009).
[7] M. Zirkl, A. Haase, A. Fian, G. Jakopic, G. Leising, B. Stadlober, I. Graz, N. Gaar, R. Schwödiauer, S. Bauer-Gogonea, and S. Bauer, Adv. Mater. **19**, 2241 (2007).
[8] A. V. Bune, V. M. Fridkin, S. Ducharme, L. M. Blinov, S. P. Palto, A. V. Sorokin, S. G. Yudin, and A. Zlatkin, Nature (London) **391**, 874 (1998).
[9] D. Rollik, S. Bauer, and R. Gerhard-Multhaupt, J. Appl. Phys. **85**, 3282 (1999).

[10] I. Graz, M. Krause, S. Bauer-Gogonea, S. Bauer, S. P. Lacour, B. Ploss, M. Zirkl, B. Stadlober, and S. Wagner, J. Appl. Phys. **106**, 034503 (2009).
[11] B. Ploss, B. Ploss, F. G. Shin, H. L. W. Chan, and C. L. Choy, Appl. Phys. Lett. **76**, 2776 (2000).
[12] P. Güthner and K. Dransfeld, Appl. Phys. Lett. **61**, 1137 (1992).
[13] K. Kimura, K. Kobayashi, H. Yamada, T. Horiuchi, K. Ishida, and K. Matsushige, Appl. Phys. Lett. **82**, 4050 (2003).
[14] K. Matsushige, H. Yamada, H. Tanaka, T. Horiuchi, and X. Q. Chen, Nanotechnology **9**, 208 (1998).
[15] B. J. Rodriguez, S. Jesse, S. V. Kalinin, J. Kim, S. Ducharme, and V. K. Fridkin, Appl. Phys. Lett. **90**, 122904 (2007).
[16] C. Rankin, C.-H. Chou, D. Conklin, and D. A. Bonnell, ACS Nano **1**, 234 (2007).
[17] T. Nishio, Y. Miyato, K. Kobayashi, K. Ishida, K. Matsushige, and H. Yamada, Nanotechnology **19**, 035202 (2008).
[18] B. W. Peterson, S. Ducharme, V. M. Fridkin, and T. J. Reece, Ferroelectrics **304**, 51 (2004).
[19] M. Zirkl, B. Stadlober, and G. Leising, Ferroelectrics **353**, 173 (2007).
[20] B. Stadlober, H. Schön, J. Groten, M. Zirkl, and G. Jakopic, in *Organic Electronics in Sensors and Biotechnology*, edited by R. Shinar and J. Shinar (McGraw-Hill, New York, 2009).
[21] A. Gruverman, in *Nanoscale Phenomena in Ferroelectric Thin Films*, edited by S. Hong (Kluwer Academic, Norwall, USA, 2004).
[22] C. Harnagea and A. Pignolet, in *Nanoscale Characterization of Ferroelectric Materials*, edited by M. Alexe and A. Gruverman (Springer-Verlag, Berlin, New York, 2004).
[23] J. Groten, Diploma Thesis, Karl-Franzens University Graz, 2008.
[24] S. V. Kalinin and D. A. Bonnell, Phys. Rev. B **63**, 125411 (2001).
[25] D. Setiadi and P. P. L. Regtien, Ferroelectrics **173**, 309 (1995).